Journal of Power Sources 691 (2026) 240933

Contents lists available at ScienceDirect

Journal of Power Sources

journal homepage: www.elsevier.com/locate/jpowsour

Exploring the potential of graphite recycling and reuse for more sustainable lithium-ion batteries

Elias Vollert [a,b], Mayokun Olutogun [a,b], Kerli Liivand [c], Thomas Diemant [a], Markus Binder [a,b], Dominic Bresser [a,b,d,*]

[a] Helmholtz Institute Ulm (HIU), Ulm, 89081, Germany
[b] Karlsruhe Institute of Technology (KIT), Karlsruhe, 76021, Germany
[c] National Institute of Chemical Physics and Biophysics (NICPB), Tallinn, 12618, Estonia
[d] Ulm University (UUlm), Ulm, 89069, Germany

HIGHLIGHTS

- Refurbishment of spent graphite for reuse in lithium-ion batteries.
- Impurities in recycled graphite promote soft short circuits.
- Acid leaching and thermal treatment remove impurities without structural changes.
- Purified graphite improves reversible capacity and ICE.
- Capacity retention of >80% after 500 cycles in graphite||NMC622 full-cells.

ARTICLE INFO

Keywords:
Recycling
Sustainability
Graphite
Anode
Lithium-ion battery

ABSTRACT

To achieve more sustainable lithium-ion batteries (LIBs), it is crucial to minimize the dependence on critical resources by maximizing their successful recovery. This study focuses on the treatment of graphite extracted from used commercial LIBs, which is commonly simply burnt off or used as fuel for the recycling of the comprised metals, to enable its reuse in the production of new LIBs. After physical separation, however, graphite contains various impurities originating from the electrolyte, separator, and cathode. Subsequent acid and heat treatments effectively reduce the amount of these impurities without causing significant structural changes to the graphite itself. As a result, the developed process leads to a noteworthy enhancement in cycling stability. The thus treated reused graphite provides a reversible capacity of 358 mAh g^{-1}, along with an initial Coulombic efficiency (CE) of nearly 90%, i.e., values that are very well competitive with pristine graphite. When used in graphite||NMC_{622} cells, it delivers very good cycling performance with a capacity retention of 80% after more than 500 cycles. These findings highlight the potential of reusing graphite as a viable pathway for more sustainable LIBs.

1. Introduction

Since their introduction by Sony in 1991, lithium-ion batteries (LIBs) have been primarily used in mobile devices like cameras, power tools, and mobile phones [1]. However, with advancements in power and energy density, cost reductions, and a growing demand for renewable energy integration, LIBs are now also being employed in larger scale applications such as electric cars, trucks, and stationary energy storage, where much larger batteries are required [2–6]. As a result, the annual production of LIBs has seen a significant increase, and is projected to reach around 3 TWh by 2030, a sixfold increase from 0.5 TWh recorded in 2020 [7]. This trend highlights the growing need for recycling, given the mounting waste generated during the manufacturing process and the growing number of batteries reaching their end-of-life [8]. By establishing recycling facilities, preferentially close to the LIB production sites, costs and raw material shortages can be reduced while simultaneously obtaining a more sustainable battery production [9,10].

It is worth noting that graphite, which is the most widely used anode

* Corresponding author. Helmholtz Institute Ulm (HIU), Ulm, 89081, Germany.
E-mail address: dominic.bresser@kit.edu (D. Bresser).

https://doi.org/10.1016/j.jpowsour.2026.240933
Received 30 March 2026; Received in revised form 5 June 2026; Accepted 7 July 2026
Available online 9 July 2026

material, is not recycled in significant quantities today [11]. In fact, graphite was classified as a critical raw material by the EU as early as 2011 [12]. This is particularly significant given China's dominance in production, accounting for 69% of the global output [13]. Despite this, recycling nowadays still prioritizes the recovery of valuable metals like Li, Co, Ni, Mn, Al, and Cu from the cathode and the current collectors [4,11,14,15]. There are three primary methods for recycling spent LIBs.

(i) The pyrometallurgical process, where the battery is stripped, and the inner components are placed in a smelter at temperatures of around 1450 °C. This process burns organic materials, including solvents, electrolytes, and plastics. Graphite serves as a reducing agent or heat source, i.e., is destroyed entirely in this process. Pre-sorting of components is possible, but this mainly applies to the Al and Cu foil, as well as plastic and steel components [10,14,16,17].

(ii) The hydrometallurgical process, where the battery materials are dissolved by acid or base leaching, followed by various purification steps. However, due to the strong chemicals used in this process, recycling graphite in sufficient quality and quantity is not possible. Only filtration can be used to recover lower-quality graphite from the remains, which is unsuitable for the application in new LIBs [11,18,19].

(iii) Direct recycling, which is the only approach that preserves the functional structure of cathode and anode active materials for potential reuse. One approach involves the flotation method, which leverages the varying hydrophobic properties of the cathode active material and graphite to facilitate their separation [10,11,14,15,20–22]. Efforts to improve this process such as cryogenic grinding [23] or the incorporation of the Fenton reagent [24] have yet to yield sufficient purity or recovery rates as the graphite used in LIBs has a purity level of 99.9%, which is consequently the benchmark for recycled graphite [14].

The main objective of the present work was the extraction of graphite from spent smartphone LIBs through physical separation, followed by purification via acid and heat treatment. Electrochemical characterization was performed after each step. The results indicate that the aforementioned treatments greatly improve the cycling stability and Coulombic efficiency. As a result, the purified graphite presents a comparably good and ecologically more sustainable alternative to primary graphite sources for the production of LIBs.

2. Experimental

2.1. The recycling process

In this study, graphite was extracted from spent LIBs obtained from Apple iPhones (series APN: 616-00036) using the multi-step process illustrated in Fig. 1. The initial stages of battery recycling were performed according to the procedure outlined by Liivand et al. [25]. To ensure safe disassembly, the batteries underwent a discharge process utilizing a 20% NaCl (Lachner, Neratovice, Czech Republic) solution. The batteries were manually disassembled and separated into anodes, cathodes, separators, and outer shells. The anodes were then immersed in *N*-methyl-2-pyrrolidone (NMP, Sigma Aldrich, Germany, 99%) to separate the graphite from the binder and copper current collector. This step was accelerated by heating the mixture to 90 °C for 30 min and applying sonication for 60 min. Finally, the graphite was filtered, washed with ethanol and de-ionized water, and dried at 75 °C.

The graphite recovered from the recycling process (rGr) was used for morphological and electrochemical characterization. Subsequently it was immersed in a 2M sulfuric acid (H_2SO_4) solution for 24 h, followed by washing with demineralized water to remove acid residues, and centrifugation. This process was repeated five times until a neutral pH (~7) was reached. In the final washing step, ethanol was used instead of water. Following this procedure, the graphite was air-dried at 80 °C for 48 h. The acid-treated graphite (rGr-AT) was subjected to the same morphological and electrochemical analyses as rGr. In the final step, rGr-AT was subjected to a heat treatment in a furnace (SAFTherm, single zone tube furnace) under an inert argon atmosphere at 850 °C for 10 h, with a constant gas flow and a ramp-up time of 3 h (4.6 °C per minute). The heat-treated graphite (rGr-HT) was then analyzed and compared to the previous results.

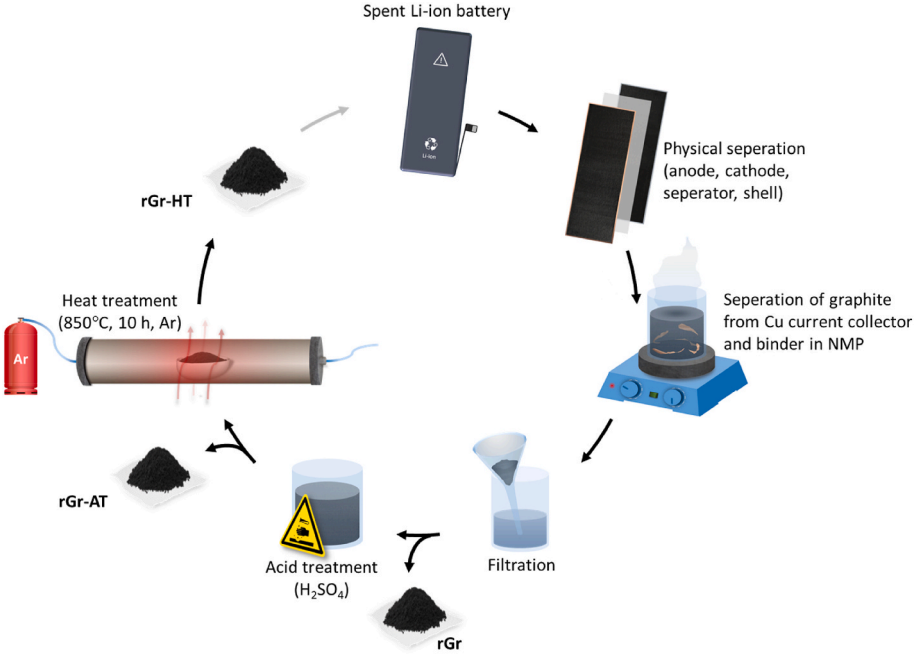

Fig. 1. Schematic illustration of the recycling process, highlighting the intermediate products rGr and rGr-AT obtained after filtration and sulfuric acid treatment, respectively. The final product (rGr-HT) shows high potential for reuse in new LIB cells.

2.2. Physiochemical characterization

The morphological analysis was carried out using a scanning electron microscope (SEM, Zeiss LEO 1550VP or Zeiss Crossbeam 340) at an accelerating voltage of 5 kV. The surface chemical composition of the samples was examined via energy-dispersive X-ray spectroscopy (EDX). The crystal structure information was obtained via powder X-ray diffraction (XRD) using a Bruker D8 Advance diffractometer (Cu Kα1 radiation, $\lambda = 0.154$ nm). The diffractograms were acquired over a 2θ range from 10° to 80°, with 0.03° step size and a step time of 9.5 s. The specific surface area was determined via nitrogen adsorption using an Autosorb-iQ (Quantachrome), following the Brunauer-Emmett-Teller method (BET) for the linear adsorption regime. The composition of the samples with regard to certain elements (Al, Cu, Co, Fe, Li, Na, and S) was analyzed using inductively coupled plasma optical emission spectroscopy (ICP-OES, Spectro Arcos). To determine the concentrations of these elements, 20 mg of the sample was dissolved in 25 mL aqua regia (HNO_3:HCl in a 3:1 ratio), filtered, and appropriately diluted to match the calibration and detection range of the elements.

X-ray photoelectron spectroscopy (XPS) was performed with monochromatic Al-Kα radiation (300 W, 13 kV) on a Specs XPS system. The survey scans were recorded with a pass energy of 90 eV. For the detail measurements, the pass energy was either set to 30 eV for the C1s and O1s region or to 60 eV for the other elements with lower concentration (in order to increase the intensity). The obtained results were analyzed using CasaXPS software. In the C1s region, an asymmetric peak shape was used for the fit of the sp^2-C contribution, which was adopted from an additional experiment with a pure graphite powder sample where C-H, C-O, or C=O species should have only a negligible concentration.

2.3. Electrode preparation

To fabricate the anode electrode sheets, the recycled graphite samples (rGr, rGr-AT or rGr-HT), styrene-butadiene rubber (SBR, TRD102A, JSR Micro), conductive carbon (C-NERGY Super C45, Imerys), and sodium carboxymethyl cellulose (CMC, Walocel CRT 2000 GA 07, degree of substitution 0.7, Dow Wolff Cellulosics) were mixed with a weight ratio of 95:3:1:1 using a planetary mixer (Thinky ARE-250). To attain a homogeneous and viscous slurry, the mixture was supplemented with deionized water, yielding a slurry composed of 40 wt% solids and 60 wt % water. The slurry was then cast on copper foil (Schlenk) using a doctor blade and subsequently dried at 80 °C. Circular electrodes with a diameter of 12 mm were punched from the coated foil and further dried under vacuum (~10^{-3} Pa) at 110 °C for 20 h. The electrodes exhibited an average active material mass loading of about 3 mg cm^{-2}, corresponding to an areal capacity of 1 mAh cm^{-2}. The average electrode density was 0.75 g cm^{-3}.

For manufacturing of the cathode, $Li[Ni_{0.6}Mn_{0.2}Co_{0.2}]O_2$ (NMC_{622}) with an average particle size of 10 μm (BASF) was mixed with conductive carbon (C-NERGY Super C65, Imerys) and polyvinylidene fluoride (PVdF 6020, Solvay) with a weight ratio of 92:4:4 in *N*-methyl-2-pyrrolidone (NMP, Sigma-Aldrich). The resulting slurry was cast on an aluminum foil using a doctor blade and dried at 80 °C. Electrodes with a diameter of 12 mm were punched out of the coated aluminum foil and then dried under vacuum (~10^{-3} Pa) at 110 °C for 20 h.

2.4. Electrochemical characterization

The electrochemical characterization in half-cells was performed using Swagelok T-cells with a three-electrode setup. The working electrodes consisted of the respective recycled graphite active material, the counter and reference electrodes were fabricated using lithium metal foils (Honjo, thickness 500 μm, lithium battery grade). The three electrodes were physically separated by a GF/D glass fiber filter from Whatman (thickness 0.67 mm, pore size 2.7 μm). The battery cells contained 300 μL of electrolyte (Solvionic), composed of 1M $LiPF_6$ in ethylene carbonate and diethyl carbonate (EC:DEC = 1:1 v/v), with 10 wt% fluoroethylene carbonate (FEC) and 2 wt% vinylene carbonate (VC) as additives to enhance the formation of a favorable solid electrolyte interphase (SEI) and, consequently, the cycling performance [26–29].

For the evaluation in full-cells, CR2032 coin cells (Hohsen) were used. The anode consisted of rGr-HT with an areal capacity of 1.3 mAh cm^{-2}, paired with a NMC_{622} cathode at an N:P ratio of 1.15. The separator, supplied by Asahi Kasei, was made of polyethylene with a thickness of 10 μm. We used 180 μL of LP30 (Solvionic, 1M $LiPF_6$ in 1:1 v/v EC:DMC) with 2 wt% VC as electrolyte.

All cells were assembled in an argon-filled glove box (MB200B ECO, MBraun, $O_2 < 0.1$ ppm and $H_2O < 0.1$ ppm) to prevent any exposure to air or moisture. A 12 h rest period was applied prior to testing to ensure thorough electrolyte wetting. Half-cell cycling followed a standardized protocol: The first cycle at C/20, the second at C/10, followed by five cycles at C/5 (cycles 3–7), then five cycles at C/2 (cycles 8–12), and from cycle 13 onward, cycling at 1C. The lower and upper cut-off voltages were set to 0.01 V and 1.0 V, respectively. The charging process employed a constant current (CC) step, while the discharge process utilized a constant current followed by a constant voltage (CCCV) step (except for the 1st discharge). The constant voltage step was maintained until the current decreased to one-tenth of the CC for the individual step. For the full-cells, the initial cycle was performed at C/20, with subsequent cycling conducted at C/2. Charging involved a constant current step until reaching an upper cut-off voltage of 4.2 V followed by a constant voltage step until the current dropped to one-tenth of the current specified for the step (CCCV charge), while discharging utilized a constant current (CC) step to a lower cut-off voltage of 2.5 V. A charge/discharge rate of 1C corresponds to 350 mA g^{-1} for graphite in half-cells and 170 mA g^{-1} for NMC_{622} in full-cells. Long-term cycling was conducted at 20 ± 2 °C using a Maccor Series 4300 Battery Tester.

Electrochemical impedance spectroscopy (EIS) measurements were performed during the first discharge cycle at 50 mV after a 1 h relaxation period. The measurements were carried out in a three-electrode setup over a frequency range from 100 kHz to 10 Hz using a sinusoidal voltage amplitude of ±10 mV.

3. Results and discussion

3.1. Physiochemical characterization of rGr, rGr-AT, and rGr-HT

The SEM micrographs in Fig. 2a and b show the recovered graphite particles (rGr) prior to the sulfuric acid and heat treatments. The graphite particles exhibit a flake-like morphology with angular features, ranging from approximately 5 to 40 μm in size. The specific BET surface area of this graphite was measured to be 4.5 m^2 g^{-1}. The SEM and EDX analysis reveals the presence of impurities. These impurities vary in chemical composition and morphology. Some appear as agglomerates of fine particles forming large, flake-like structures with a rough surface and a size of about 10 to 50 μm, as shown in Fig. 2c. EDX analysis indicates that they are composed primarily of carbon and oxygen. Their surface texture and composition suggest that they are agglomerates of conductive carbon. Fig. 2d–f depict the other types of impurities. These include impurities present as smaller particles attached to the surface of the graphite particles, composed of aluminum and oxygen or rich in fluorine. The impurities composed of aluminum and oxygen likely originate from the separator's ceramic coating (Al_2O_3). Ceramic coatings are commonly employed to enhance thermal stability and wettability [30]. The fluorine-rich impurities are likely fluoride salts such as, e.g., LiF. As described by Andersson and Edström [31], these can arise from the decomposition reaction of the electrolyte conductive salt, presumably $LiPF_6$. Especially trace water can promote the formation of LiF. In addition, ICP-OES analysis confirmed the presence of further trace impurities. Table 1 shows the presence of metals such as Na, Co, Al, and Li, together accounting for 0.17 wt.%. Li and Co are presumably originating

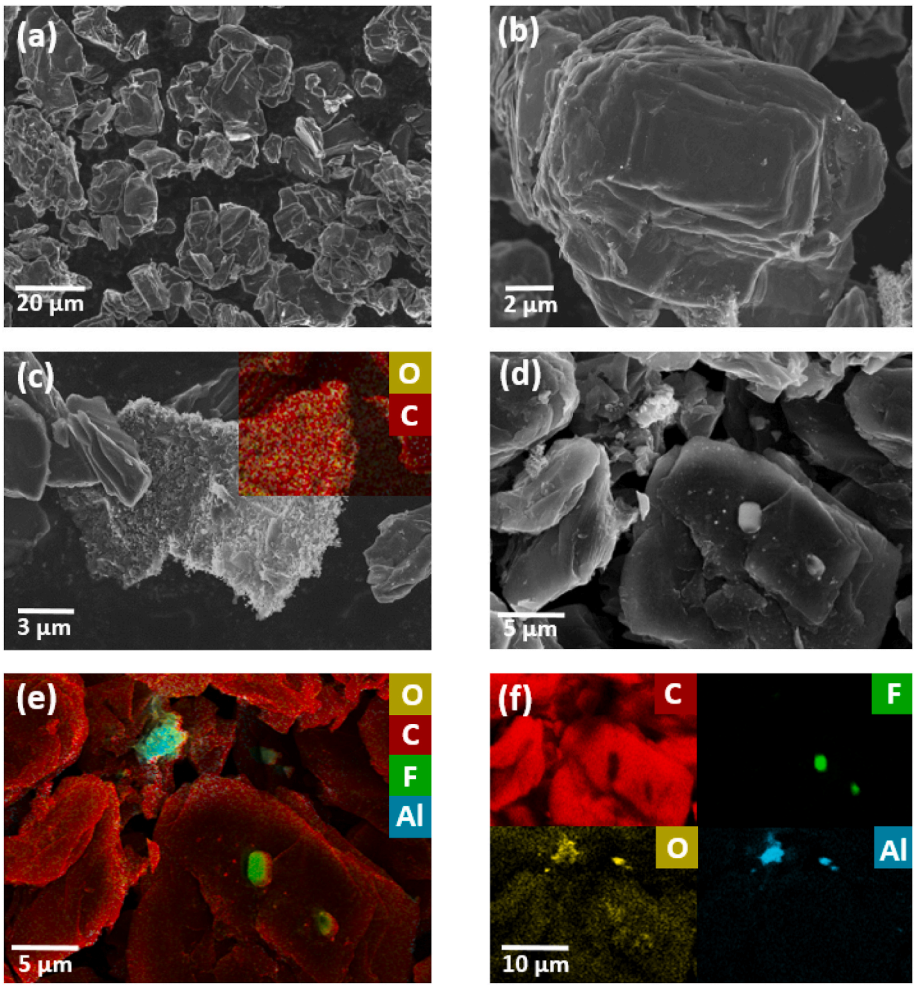

Fig. 2. Morphological characterization of rGr: (a, b) SEM micrographs at different magnifications, showing particles ranging from approximately 5 to 40 µm in size. (c) High-magnification micrograph of a flake-like impurity, with the EDX mapping as inset, showing a homogeneous distribution of oxygen (yellow) and carbon (red). (d) SEM micrograph and (e, f) the corresponding EDX maps, highlighting impurities composed of aluminum (turquoise) and oxygen (yellow) or fluoride (green). (For interpretation of the references to colour in this figure legend, the reader is referred to the Web version of this article.)

Table 1
Quantification of the impurities for rGr, rGr-AT, and rGr-HT using ICP-OES. Values below the detection limit are designated as n.d. (<0.001).

Element	Concentration rGr [wt.%]	Concentration rGr-AT [wt.%]	Concentration rGr-HT [wt.%]
Na	0.042	0.023	0.014
Co	0.040	n.d.	n.d.
Al	0.035	n.d.	0.003
Li	0.033	n.d.	n.d.
S	0.012	0.023	0.012
Cu	0.005	n.d.	n.d.
Fe	0.002	n.d.	0.010
Σ	**0.169**	**0.046**	**0.039**

from the cathode active material, and the absence of manganese and nickel suggests that $LiCoO_2$ has been used as the cathode active material for these LIBs. Finding them attached as small particles to graphite indicates that they either stem from cross-talk phenomena occurring during cycling or the recycling process [32].

After sulfuric acid treatment, the SEM micrographs (Fig. 3a and b) show a clear reduction in impurities. Before the acid treatment (rGr), nearly all graphite particles contained impurities. In contrast, after treatment (rGr-AT) most particles were free of surface deposits. Only a small fraction of graphite particles displayed a high concentration of impurities as shown in Fig. 3c and d. Importantly, such deposits were not observed on rGr, i.e., prior to the acid treatment. Hence, it is reasonable to attribute these to reaction products of the sulfuric acid, which is in line with a relatively higher sulfur concentration detected for these samples via ICP-OES (Table 1). Besides, the ICP-OES analysis confirmed a significant reduction of undesirable elements, with concentrations below the detection limit. This observation is consistent with the SEM results. Additionally, a slight decrease of the BET surface area was observed, viz., from 4.5 to 4.2 $m^2\ g^{-1}$ (−5.5%). This reduction is likely due to the effective removal of surface impurities. After the subsequent heat treatment, the remaining impurities were further removed, as clearly visible from the corresponding SEM and ICP-OES results (Fig. S1 and Table 1). The heat treatment in an argon atmosphere resulted in a substantial increase of the BET surface area, reaching 11.4 $m^2\ g^{-1}$. This increase presumably originates from the decomposition of residual binder during the heat treatment, which unblocks previously obstructed pores and decreases the overall particle agglomeration [33–37].

Despite these changes, no significant structural alterations were observed, as evident from the XRD analysis of rGr, rGr-AT, and rGr-HT (Fig. S2a). The diffractograms for all three samples exhibit no significant disparities in the position and intensity of the reflections. The main feature at 26.5° corresponds to an interlayer distance of 3.37 Å, which is slightly higher than the typical distance of around 3.35 Å reported for graphite [38]. This observation indicates an increase of the interlayer distance owing to the repeated galvanostatic cycling of the battery cells [32,39].

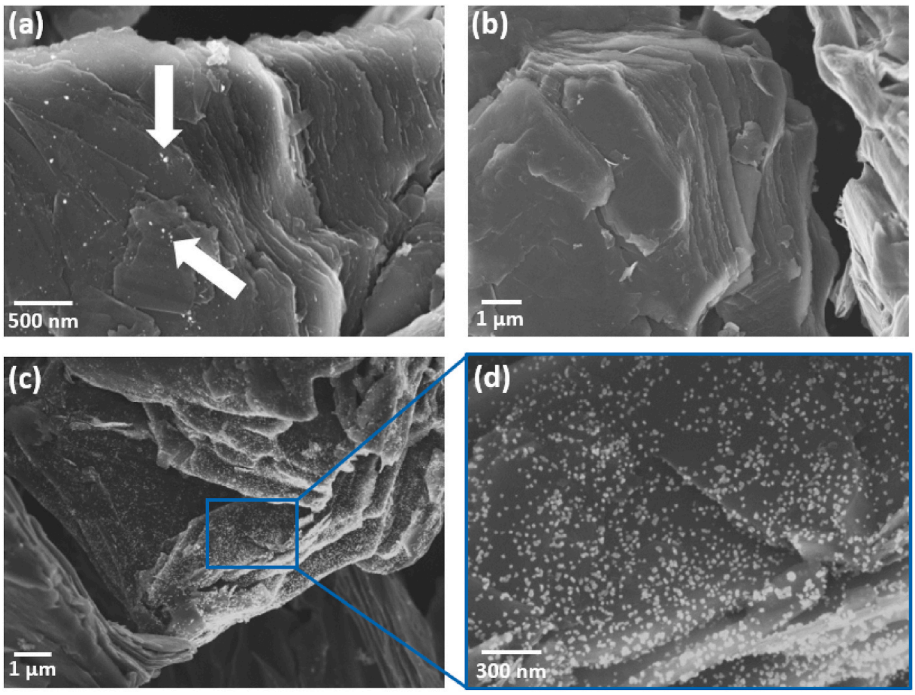

Fig. 3. SEM micrographs of graphite particles before and after H_2SO_4 treatment: (a) Close-up SEM micrograph of a graphite particle prior to the treatment, and (b) after the treatment, showcasing the removal of fine impurities. (c) SEM micrograph of an area on the treated graphite particles with a localized accumulation of impurities and (d) close-up of these rare impurity clusters observed for rGr-AT.

Notably, the interlayer spacing remains essentially unchanged across the three samples, with only a slight decrease (i.e., a subtle shift to higher diffraction angles) observed after heat treatment (Fig. S2b). Overall, these results suggest that neither sulfuric acid treatment nor the subsequent thermal treatment lead to significant structural changes of the graphite framework.

Further chemical analysis of the different graphite samples was conducted using XPS to investigate the impact of acid and heat treatments on the surface composition. The C 1s spectra (Fig. 4a,c,e) display the characteristic graphite signal, with a dominant asymmetric peak at 284.5 eV, corresponding to sp^2-hybridized carbon. The peaks at higher energies indicate heteroatom-containing species, viz., C–O at 286.5 eV and carbonyl groups (C=O) at 288.8 eV. Additionally, the π-π* satellite peak, which is commonly observed in XPS measurements of conductive carbon samples, was found at 290.9 eV [40,41]. The peaks at 531.9 and 533.5 eV in the O 1s spectra (Fig. 4b,d,f) correspond to the presence of C=O and C-O species, respectively. The O 1s spectrum of rGr generally displays a higher intensity compared to rGr-AT and rGr-HT, indicating a significantly higher content of oxygen-containing species on the surface with a total of 4.0 at.%, in comparison to 2.8 at.% and 1.3 at.% for rGr-AT and rGr-HT, respectively (Table S1). Furthermore, the O 1s spectrum of rGr also shows a significantly stronger intensity of the peak at 531.9 eV. This can partly be explained by a higher number of impurities in addition to carbon-oxygen compounds within the sample. Impurities like metal hydroxides, aluminum oxide, or sulfates exhibit binding energies of around 531.5 eV [41–45]. This creates a spectral overlap with carbonyl groups, preventing a definitive differentiation between the surface functional groups and residual contaminants. Furthermore, signal intensity at lower binding energy (530.0 eV) is attributed in the case of r-Gr to cobalt oxide [46]. The sulfuric acid treatment markedly reduced the intensity of the carbonyl (C=O) peak. This effect can mostly be related to the removal of impurities, since dilute sulfuric acid is not strongly oxidizing. It may still induce minor oxygen functionalization and can, under certain conditions, promote weak intercalation and slight lattice expansion, but it is generally insufficient to cause substantial oxidation or full exfoliation of the graphite structure alone as seen by the overall net removal of oxygen species in XPS (Fig. 4d and Table S1) and the absence of any significant change in the XRD pattern (Fig. S2a) [47].

The subsequent heat treatment leads to a further reduction of the oxygen content to 1.3 at.%. For comparison, we carried out an XPS analysis also for a pristine commercial graphite material (Fig. S3, Table S2). The same heat treatment as for the recovered graphite materials yielded a reduction of the surface oxygen groups from 2.6 at.% to 0.8 at.%. This observation suggests that the primary impact of the heat treatment is the reduction of oxygen groups on the graphite surface, as opposed to a primarily reduction in oxygen containing impurities. It is well established in the literature that heat treatments at around 850 °C, as applied in this study, lead to the removal of surface oxygen species. In particular, surface groups such as carboxyl (-COOH), observed at around ~531.7 eV (C-O) and ~533.1 eV (C=O), anhydrides (-CO-O-CO-) at ~532.4-532.6 eV, and epoxides (C-O-C) at ~533.1 eV, are thermally less stable and are released predominantly as CO_2, with smaller amounts of CO [48–51]. This process generally transforms pre-existing oxygen induced defects into vacancies, i.e., Stone-Wales defects, since a temperature of 850 °C is generally insufficient to induce significant recrystallization of the sp^2 graphitic lattice. Such recrystallization typically would require temperatures of 1600 °C or higher [52,53]. The removal of heteroatoms is critical, as it lowers the catalytic activity towards SEI formation [50]. In particular, C=O groups are known to promote excessive SEI formation, as shown in simulations by Leung and Budzien [54].

3.2. Electrochemical characterization in half-cells

The electrochemical performance of electrodes based on the three different graphite materials was first studied in half-cells with a lithium-metal counter electrode. In all cases, three cells were cycled to ensure reproducibility of the data. Fig. 5 displays the specific capacity, capacity retention, and Coulombic efficiencies (CEs) over the first 140 cycles for the rGr, rGr-AT, and rGr-HT half-cells. The corresponding charge/discharge profiles are provided in Fig. S4. For rGr (Fig. 5a), an average

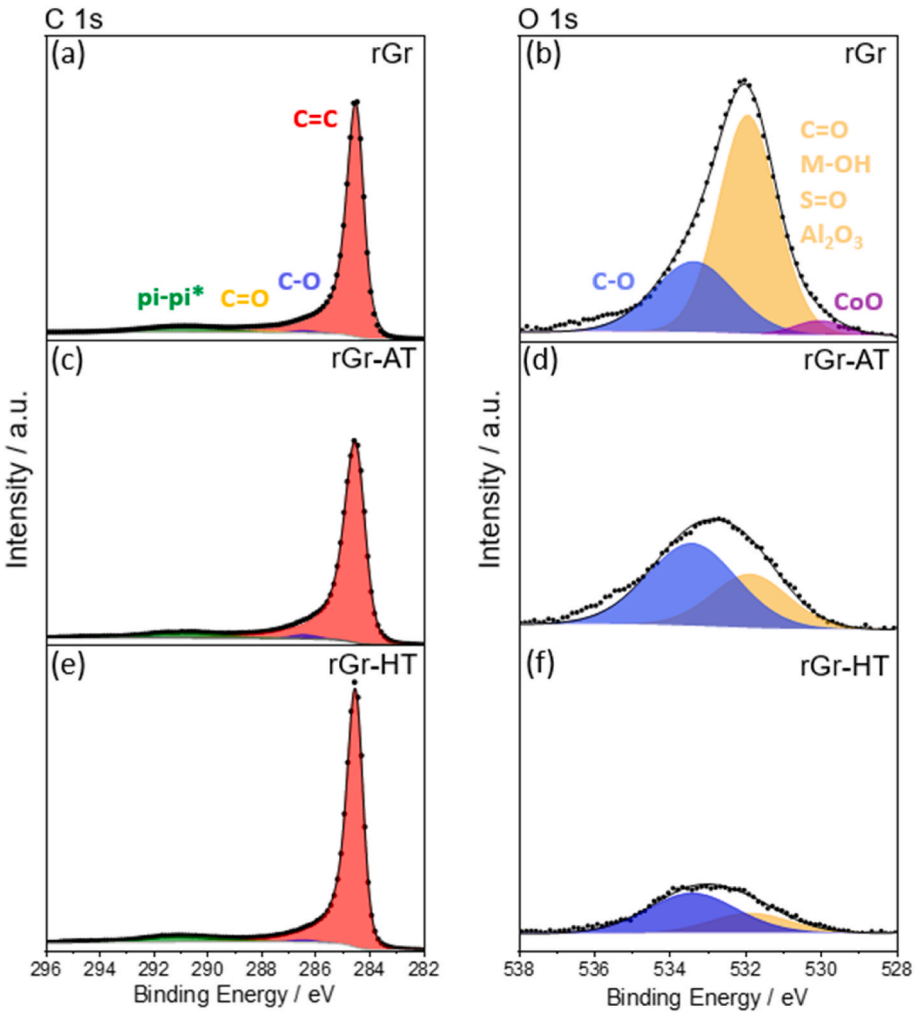

Fig. 4. XPS detail spectra in the (a, c, e) C 1s and (b, d, f) O 1s region for (a, b) rGr, (c, d) rGr-AT, and (e, f) rGr-HT.

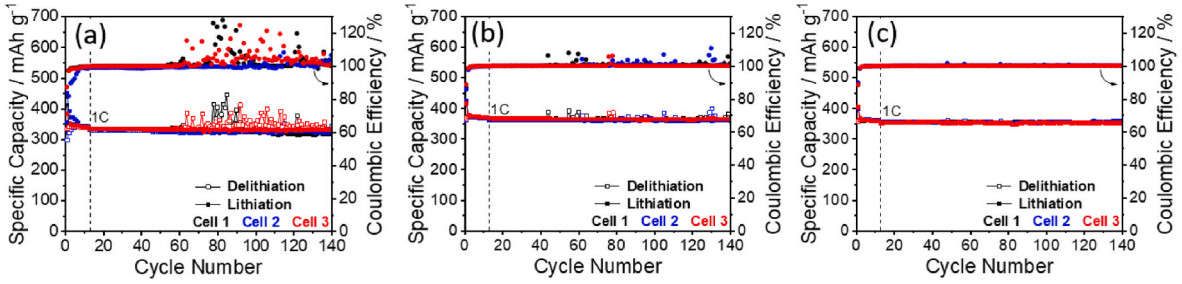

Fig. 5. Electrochemical characterization of electrodes based on (a) rGr, (b) rGr-AT, and (c) rGr-HT in half-cells using a three-electrode setup with lithium metal as counter and reference electrodes. The cells were cycled in a potential window between 0.01 V and 1.0 V vs. Li^+/Li at a charge/discharge rate of 1C (350 mA g^{-1}) after the formation cycles (including a CCCV step upon lithiation after the first cycle; see the Experimental section for more details).

initial reversible specific capacity of 324 mAh g^{-1} was obtained, as detailed in Table 2. The values show a considerable variability concerning the standard deviation (SD), and are significantly lower than those typically achieved with commercial graphite [55,56]. Together with a high initial discharge capacity, this results in a relatively low and inconsistent initial CE (ICE) of about 78%. During the long-term cycling test, the discharge capacities and CEs remain relatively stable up to approximately the 60th cycle. However, beyond this point, a substantial fluctuation of the charge capacity emerges, rendering the plots very "noisy" and resulting in CEs surpassing 100%. rGr-AT (Fig. 5b) shows a significant improvement over rGr with an average reversible capacity of 366 mAh g^{-1}, an average ICE of 87%, and substantially reduced capacity fluctuations. Nevertheless, fluctuations persist beyond cycle 50 for all cells, though to a lower extent. The subsequent heat treatment under argon atmosphere (rGr-HT, Fig. 5c) results in the complete elimination of the charge potential fluctuations and a further increase of the ICE to an average of 89%. This effect is primarily attributed to a reduction of the first-cycle discharge capacity, which drops by 20 mAh g^{-1} from 421 mAh g^{-1} (rGr-AT) to 401 mAh g^{-1} (r-Gr-HT), while the average charge capacity only decreases from 366 to 358 mAh g^{-1} (−8 mAh g^{-1}) (see Table 2). These observations correlate with the EIS results presented in Fig. S5 and Table S3. The high irreversible capacity loss of untreated rGr

Table 2
Comparison of the first-cycle specific discharge capacities, the reversible specific capacities obtained upon the first charge, i.e., delithiation, the initial Coulombic efficiencies (ICEs), and discharge capacity at the 100th cycle for rGr, rGr-AT, and rGr-HT half-cells tested at C/20. The reported values represent averages from three independent cells per sample and include the standard deviation (SD).

Sample	1st cycle specific discharge capacity [mAh g^{-1}]	1st cycle reversible specific capacity [mAh g^{-1}]	ICE [%]	100th cycle specific discharge capacity [mAh g^{-1}]
rGr	417 (±29)	324 (±18)	78 (±9)	327 (±4)
rGr-AT	421 (±3)	366 (±2)	87 (±1)	363 (±2)
rGr-HT	401 (±1)	358 (±1)	89 (±1)	353 (±1)

is in line with its elevated SEI layer resistance (R1 = 26 Ω) and charger transfer resistance (61 Ω), reflecting a thicker and less conductive interphase. In contrast, due to the purification process rGr-AT and rGr-HT allows for a more efficient and conductive SEI being formed during the first cycle, achieving lower interphase resistances (R1 = 16 Ω for rGr-AT and R1 = 14 Ω for rGr-HT), as well as reduced charge transfer resistances (R2 = 24 Ω for rGr-AT and R1 = 29 Ω for rGr-HT).

Notably, the reduction of the first-cycle discharge capacity occurred despite a significant increase of the BET surface area. These findings suggest that the BET surface area plays a less dominant role in this case compared to previous studies by Olivier et al. [57] and Winter et al. [58] when comparing different pristine graphite materials. These studies proposed a linear relationship between BET surface area and the first-cycle irreversible capacity. Our results for the recycled graphite, though, indicate that in this case other factors influence the discharge capacity of recycled graphite more strongly. One potential explanation for the lower discharge capacity for rGr-HT is the reduction in side reactions between the anode and the electrolyte owing to the presence of oxygen-containing surface species, as well as the removal of the sulfur-containing impurities that were deposited during the H_2SO_4 treatment. This cleaning process is crucial in minimizing the occurrence of side reactions at the electrode|electrolyte interface. Consequently, this leads to a noticeable decrease of the initial discharge capacity. We may also note that the first-cycle reversible specific capacity upon delithiation experiences a decrease to an average of 358 mAh g^{-1}, which still remains comparable to pristine commercial graphite (cf. Fig. 6a), though. At least as important, the SD is gradually decreasing from rGr over rGr-AT to rGr-HT, further underlining how the applied treatments lead to a homogeneously cleaned-up active material. After 100 cycles, rGr-HT still retains 99.6% (353 mAh g^{-1}) of its original capacity compared to the 13th cycle (i.e., the first cycle at 1C). This capacity retention is well above that observed for rGr (97.6%) and somewhat higher than for rGr-AT (99.3%). It should be noted in case that this comparatively high capacities at 1C arise from the use of a CCCV protocol, in which a constant-voltage step supplements the constant-current discharge at 1C.

For further investigating the origin of the charge capacity fluctuations which are particularly present for rGr and to a lesser extent for rGr-AT, we carried out additional electrochemical tests in half-cells with the pristine commercial graphite material (SLP30) studied already via XPS (Fig. S3). The results are shown in Fig. 6. We employed two different glass fiber separators with a compressed thickness of 150 µm (GF/A) and 300 µm (GF/D) to test the hypothesis that this charge capacity fluctuations with capacities well exceeding the theoretical limit, resulting in CEs beyond the theoretical maximum of 100%, originates from the formation of so-called soft short-circuits, i.e., the detachment of lithium from the lithium-metal counter electrode surface, and subsequent diffusion to the graphite electrode surface, where these lithium-metal fragments "react" with graphite, enter into the graphite host structure, and get reoxidized to lithium ions, which are subsequently migrating back to the lithium-metal electrode. As apparent from the comparison of the specific capacity and CE plots in Fig. 6a, a charge capacity well exceeding the theoretical maximum appears already after 60 cycles in the case of the thinner separator (GF/A), while it takes around 200 cycles for the thicker separator (GF/D). This finding indicates that the diffusion of such soft-short-circuit-originating lithium fragments to the graphite electrode takes substantially longer for the thicker separator, as

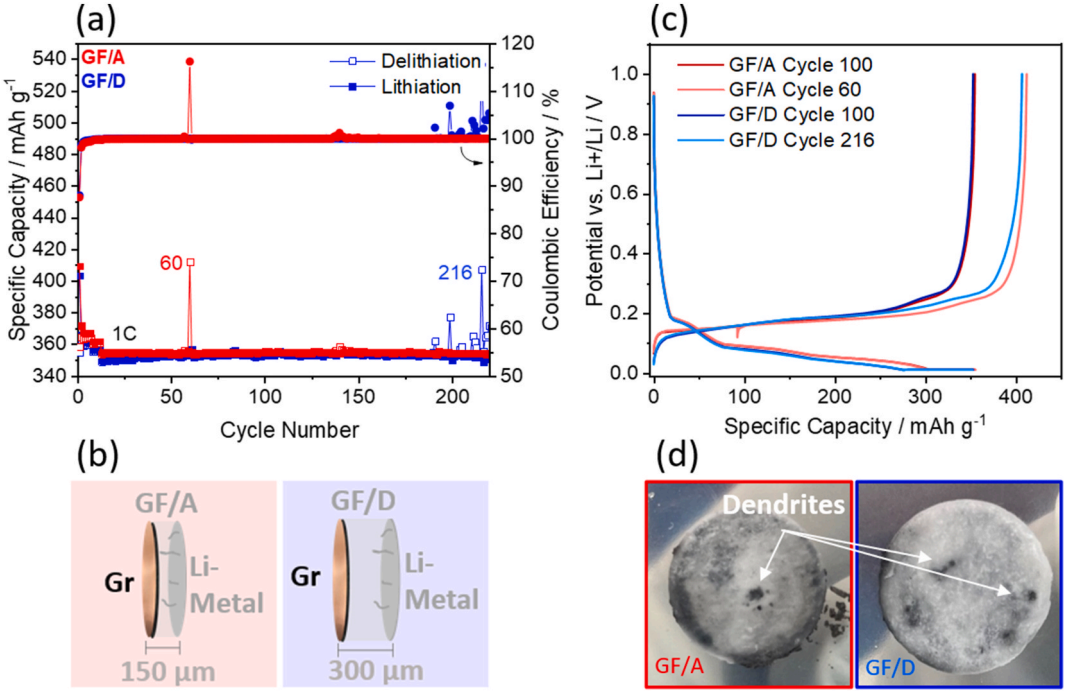

Fig. 6. (a) Galvanostatic cycling of graphite half-cells with GF/A and GF/D separators. (b) Schematic representation of dendrite formation in graphite half-cells with the two different glass fiber separators GF/A and GF/D. (c) Selected voltage profiles for the 60th and 100th cycle when using GF/A and the 100th and 216th cycle when using GF/D as separator. (d) Photographs of the separators extracted from the cycled cells, highlighting the formation of dendrites, piercing the separator.

schematically illustrated in Fig. 6b, thus, corroborating our hypothesis. Further confirmation is provided by the plot of the galvanostatic cycling profiles for which such elevated charge capacities are observed, depicted in Fig. 6c, revealing the characteristic profile for graphite – only with an "elongated" delithiation process. This observation supports the hypothesis that these lithium fragments are "reacting" with graphite, resulting in lithiated graphite, and the subsequent reoxidation and deintercalation of the lithium ions from the graphite structure and their migration back to the lithium counter electrode. In fact, when disassembling these cells, we found black spots on the separators (Fig. 6d): a very large and intense one in the case of GF/A, in line with the large excess in charge capacity observed for cycle 60, and a few smaller and less intense ones in the case of GF/D, in line with the charge potential fluctuations observed for several cycles after about 200 cycles.

For the recycled graphite materials, we may assume that the presence of impurities triggers the formation of soft short circuits as a result of a destabilized SEI, favoring a less uniform lithium-ion flux and, thus, the formation of dendritic lithium structures. In fact, it has been reported that the presence of transition metals at the graphite surface leads to a degradation of the SEI, promoting a locally increased electrolyte decomposition and, as a result, a less uniform lithium-ion flux [59–61]. By reducing the impurities, especially through the sulfuric acid treatment, and further by the subsequent heat treatment, this phenomenon can be suppressed, which is reflected in the significant reduction of the charge potential fluctuations observed in Fig. 5.

3.3. Evaluation in graphite||NMC_{622} full-cells

Motivated by the excellent half-cell performance of rGr-HT, we finally assembled full-cells with a $Li[Ni_{0.6}Mn_{0.2}Co_{0.2}]O_2$ (NMC_{622}) cathode and an N:P ratio of 1.15 based on their capacities determined experimentally at C/20. Fig. 7 shows the cycling performance of these graphite||NMC_{622} full-cells. The first charge capacities (lithium ions being intercalated into the graphite negative electrode) were 194 and 192 mAh g^{-1} (referring to the cathode active material mass) and the first discharge capacities (lithium ions being reinserted into the NMC_{622} positive electrode) were 164 and 167 mAh g^{-1}, resulting in ICEs of 84.5% and 87.2% at C/20. Both full-cells exhibit highly stable cycling for more than 1000 cycles with an average CE of 99.9% and a capacity retention above 80% until the 530th cycle, thus, further corroborating our hypothesis that the charge capacity fluctuations are related to reactions occurring at the lithium-metal counter electrode for the half-cells.

4. Conclusions

The successful recycling of graphite through physical separation and subsequent acid and heat treatment has been demonstrated. The stepwise removal of impurities results in higher ICEs and the suppression of the capacity fluctuations during delithiation observed for the as-recycled graphite. The finally obtained graphite material shows a high and very stable cycling performance, enabling the realization of long-term stable graphite||NMC_{622} full-cells with a capacity retention of above 80% after more than 500 cycles and high CE of more than 99.9%. Accordingly, these results render the reuse of recycled (and properly cleaned) graphite in new LIB cells very well feasible, thus, providing a suitable path towards the development of more sustainable LIBs, while also ensuring an efficient use of the critical component graphite.

Declaration of generative AI and AI-assisted technologies in the writing process

During the preparation of this work the authors used ChatGPT 5.3 (OpenAI) and Gemini 3 (Google) to refine sentence structure and ensure grammatical accuracy. After using these tools/services, the authors reviewed and edited the content as needed and take full responsibility for the content of the published article.

CRediT authorship contribution statement

Elias Vollert: Data curation, Formal analysis, Investigation, Methodology, Visualization, Writing – original draft. **Mayokun Olutogun:**

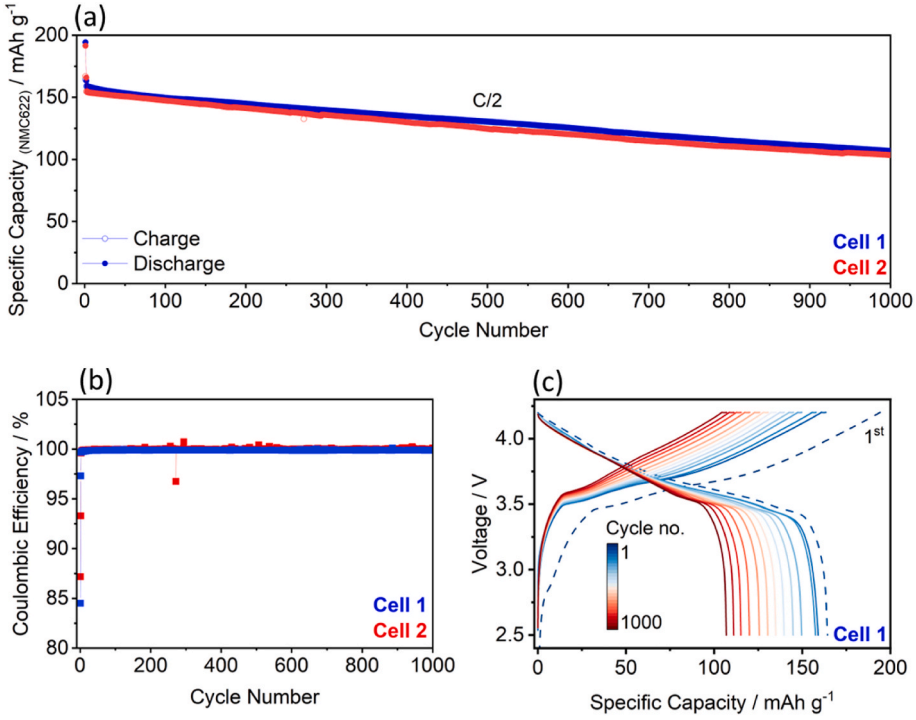

Fig. 7. Electrochemical characterization of rGr-HT||NMC_{622} full-cells with (a) a plot of the specific capacity and (b) the CE over 1000 cycles at C/2. The results obtained for two full-cells are displayed to confirm the reproducibility of the results. (c) Dis-/charge profiles of cell 1 for selected cycles from cycle 1 to cycle 1000.

Conceptualization, Data curation, Formal analysis, Investigation, Writing – review & editing. **Kerli Liivand:** Data curation, Investigation, Writing – review & editing. **Thomas Diemant:** Data curation, Investigation, Writing – review & editing. **Markus Binder:** Investigation, Writing – review & editing. **Dominic Bresser:** Conceptualization, Funding acquisition, Methodology, Resources, Supervision, Writing – review & editing.

Declaration of competing interest

The authors declare the following financial interests/personal relationships which may be considered as potential competing interests: Dominic Bresser reports financial support was provided by Federal Ministry of Education and Research Bonn Office. Kerli Liivand reports financial support was provided by Estonian Research Council. Kerli Liivand reports financial support was provided by Estonian Ministry of Education abd Research. If there are other authors, they declare that they have no known competing financial interests or personal relationships that could have appeared to influence the work reported in this paper.

Acknowledgment

The authors express their gratitude to the Federal Ministry of Research, Technology and Space (BMFTR) for providing financial support through the HighSafe project (03XP0138C), the HighSafe-2 (03XP0306C), and the HighSafe-3 (03XP0568A) project. The authors also acknowledge the financial support received from the Helmholtz Association. Additionally, this work was supported by the Estonian Research Council grant (PSG926) and by the Ministry of Education and Research through the Centre of Excellence in Circular Economy for Strategic Mineral and Carbon Resources (01.01.2024–31.12.2030, TK228).

Appendix A. Supplementary data

Supplementary data to this article can be found online at https://doi.org/10.1016/j.jpowsour.2026.240933.

Data availability

Data will be made available on request.

References

[1] G.E. Blomgren, The development and future of lithium ion batteries, J. Electrochem. Soc. 164 (2016) A5019, https://doi.org/10.1149/2.0251701jes.
[2] M. Armand, P. Axmann, D. Bresser, M. Copley, K. Edström, C. Ekberg, D. Guyomard, B. Lestriez, P. Novák, M. Petranikova, Lithium-ion batteries–current state of the art and anticipated developments, J. Power Sources 479 (2020) 228708, https://doi.org/10.1016/j.jpowsour.2020.228708.
[3] C. Curry, Lithium-ion battery costs and market, Bloom, New Energy Finance 5 (4–6) (2017) 43.
[4] B. Scrosati, K. Abraham, W.A. van Schalkwijk, J. Hassoun, Lithium Batteries: Advanced Technologies and Applications, John Wiley & Sons, 2013.
[5] D. Bresser, K. Hosoi, D. Howell, H. Li, H. Zeisel, K. Amine, S. Passerini, Perspectives of automotive battery R&D in China, Germany, Japan, and the USA, J. Power Sources 382 (2018) 176–178, https://doi.org/10.1016/j.jpowsour.2018.02.039.
[6] M. Marinaro, D. Bresser, E. Beyer, P. Faguy, K. Hosoi, H. Li, J. Sakovica, K. Amine, M. Wohlfahrt-Mehrens, S. Passerini, Bringing forward the development of battery cells for automotive applications: perspective of R&D activities in China, Japan, the EU and the USA, J. Power Sources 459 (2020) 228073, https://doi.org/10.1016/j.jpowsour.2020.228073.
[7] S. Moores, The global battery arms race: lithium-ion battery gigafactories and their supply chain, Oxf. Energy Forum 126 (2021) 26–30.
[8] L. Gaines, J. Sullivan, A. Burnham, I. Belharouak, Life-cycle analysis for lithium-ion battery production and recycling, in: Transp. Res. Board 90th Annu. Meet. Wash. DC, 2011, pp. 23–27.
[9] B. Jones, R.J. Elliott, V. Nguyen-Tien, The EV revolution: the road ahead for critical raw materials demand, Appl. Energy 280 (2020) 115072, https://doi.org/10.1016/j.apenergy.2020.115072.
[10] G. Harper, R. Sommerville, E. Kendrick, L. Driscoll, P. Slater, R. Stolkin, A. Walton, P. Christensen, O. Heidrich, S. Lambert, Recycling lithium-ion batteries from electric vehicles, Nature 575 (2019) 75–86.
[11] J. Asenbauer, T. Eisenmann, M. Kuenzel, A. Kazzazi, Z. Chen, D. Bresser, The success story of graphite as a lithium-ion anode material–fundamentals, remaining challenges, and recent developments including silicon (oxide) composites, Sustain. Energy Fuels 4 (2020) 5387–5416, https://doi.org/10.1039/D0SE00175A.
[12] European Commission, Communication from the Commission to the European Parliament, the Council, the European Economic and Social Committee and the Committee of the Regions; Tackling the Challenges in Commodity Markets and on Raw Materials, 2011.
[13] M. Grohol, C. Veeh, Study on the Critical Raw Materials for the EU 2023, 2023.
[14] B. Moradi, G.G. Botte, Recycling of graphite anodes for the next generation of lithium ion batteries, J. Appl. Electrochem. 46 (2016) 123–148, https://doi.org/10.1007/s10800-015-0914-0.
[15] M. Abdollahifar, S. Doose, H. Cavers, A. Kwade, Graphite recycling from end-of-life lithium-ion batteries: processes and applications, Adv. Mater. Technol. 8 (2023) 2200368, https://doi.org/10.1002/admt.202200368.
[16] S. Rothermel, M. Evertz, J. Kasnatscheew, X. Qi, M. Grützke, M. Winter, S. Nowak, Graphite recycling from spent lithium-ion batteries, ChemSusChem 9 (2016) 3473–3484, https://doi.org/10.1002/cssc.201601062.
[17] M. Chen, X. Ma, B. Chen, R. Arsenault, P. Karlson, N. Simon, Y. Wang, Recycling end-of-life electric vehicle lithium-ion batteries, Joule 3 (2019) 2622–2646, https://doi.org/10.1016/j.joule.2019.09.014.
[18] X. Ma, M. Chen, B. Chen, Z. Meng, Y. Wang, High-performance graphite recovered from spent lithium-ion batteries, ACS Sustain. Chem. Eng. 7 (2019) 19732–19738, https://doi.org/10.1021/acssuschemeng.9b05003.
[19] Z. Shang, W. Yu, J. Zhou, X. Zhou, Z. Zeng, R. Tursun, X. Liu, S. Xu, Recycling of spent lithium-ion batteries in view of graphite recovery: a review, eTransportation (2024) 100320, https://doi.org/10.1016/j.etran.2024.100320.
[20] J. Gao, X. Bu, L. Dong, Y. Qiu, G. Xie, S. Chehreh Chelgani, Natural graphite froth Flotation-An overview, Miner. Process. Extr. Metall. Rev. 46 (2025) 306–323, https://doi.org/10.1080/08827508.2024.2305384.
[21] M. Talebi, T. Diemant, J.-K. Kim, M. Binder, D. Bresser, Impact of residuals on recovered nickel-rich LiNi1-x-yMnxCoyO2 cathodes for direct recycling and reuse, J. Power Sources Adv 37 (2026) 100200, https://doi.org/10.1016/j.powera.2025.100200.
[22] M. Olutogun, A. Vanderbruggen, C. Frey, M. Rudolph, D. Bresser, S. Passerini, Recycled graphite for more sustainable lithium-ion batteries, Carbon Energy 6 (2024) e483, https://doi.org/10.1002/cey2.483.
[23] J. Liu, H. Wang, T. Hu, X. Bai, S. Wang, W. Xie, J. Hao, Y. He, Recovery of LiCoO2 and graphite from spent lithium-ion batteries by cryogenic grinding and froth flotation, Miner. Eng. 148 (2020) 106223, https://doi.org/10.1016/j.mineng.2020.106223.
[24] Y. He, T. Zhang, F. Wang, G. Zhang, W. Zhang, J. Wang, Recovery of LiCoO2 and graphite from spent lithium-ion batteries by Fenton reagent-assisted flotation, J. Clean. Prod. 143 (2017) 319–325, https://doi.org/10.1016/j.jclepro.2016.12.106.
[25] K. Liivand, M. Kazemi, P. Walke, V. Mikli, M. Uibu, D.D. Macdonald, I. Kruusenberg, Spent Li-Ion battery graphite turned into valuable and active catalyst for electrochemical oxygen reduction, ChemSusChem 14 (2021) 1103–1111, https://doi.org/10.1002/cssc.202002742.
[26] O. Matsuoka, A. Hiwara, T. Omi, M. Toriida, T. Hayashi, C. Tanaka, Y. Saito, T. Ishida, H. Tan, S.S. Ono, Ultra-thin passivating film induced by vinylene carbonate on highly oriented pyrolytic graphite negative electrode in lithium-ion cell, J. Power Sources 108 (2002) 128–138, https://doi.org/10.1016/S0378-7753(02)00012-5.
[27] H. Ota, Y. Sakata, A. Inoue, S. Yamaguchi, Analysis of vinylene carbonate derived SEI layers on graphite anode, J. Electrochem. Soc. 151 (2004) A1659, https://doi.org/10.1149/1.1785795.
[28] D. Aurbach, K. Gamolsky, B. Markovsky, Y. Gofer, M. Schmidt, U. Heider, On the use of vinylene carbonate (VC) as an additive to electrolyte solutions for Li-ion batteries, Electrochim. Acta 47 (2002) 1423–1439, https://doi.org/10.1016/S0013-4686(01)00858-1.
[29] I.A. Profatilova, S.-S. Kim, N.-S. Choi, Enhanced thermal properties of the solid electrolyte interphase formed on graphite in an electrolyte with fluoroethylene carbonate, Electrochim. Acta 54 (2009) 4445–4450, https://doi.org/10.1016/j.electacta.2009.03.032.
[30] R. Shomura, R. Tamate, S. Matsuda, Lithium-ion-conducting ceramics-coated separator for stable operation of lithium metal-based rechargeable batteries, Materials 15 (2022) 322, https://doi.org/10.3390/ma15010322.
[31] A.M. Andersson, K. Edström, Chemical composition and morphology of the elevated temperature SEI on graphite, J. Electrochem. Soc. 148 (2001) A1100, https://doi.org/10.1149/1.1397771.
[32] K. Liu, S. Yang, L. Luo, Q. Pan, P. Zhang, Y. Huang, F. Zheng, H. Wang, Q. Li, From spent graphite to recycle graphite anode for high-performance lithium ion batteries and sodium ion batteries, Electrochim. Acta 356 (2020) 136856, https://doi.org/10.1016/j.electacta.2020.136856.
[33] J. Zhang, X. Li, D. Song, Y. Miao, J. Song, L. Zhang, Effective regeneration of anode material recycled from scrapped Li-ion batteries, J. Power Sources 390 (2018) 38–44, https://doi.org/10.1016/j.jpowsour.2018.04.039.
[34] M.J. Lacey, F. Jeschull, K. Edström, D. Brandell, Porosity blocking in highly porous carbon black by PVdF binder and its implications for the Li–S system, J. Phys. Chem. C 118 (2014) 25890–25898, https://doi.org/10.1021/jp508137m.

[35] W. Li, H. Li, Y.-M. Zhang, Preparation and investigation of PVDF/PMMA/TiO2 composite film, J. Mater. Sci. 44 (2009) 2977–2984, https://doi.org/10.1007/s10853-009-3395-x.
[36] Y. Gao, J. Zhang, H. Jin, G. Liang, L. Ma, Y. Chen, C. Wang, Regenerating spent graphite from scrapped lithium-ion battery by high-temperature treatment, Carbon 189 (2022) 493–502, https://doi.org/10.1016/j.carbon.2021.12.053.
[37] A. Chernyaev, A. Kobets, K. Liivand, F. Tesfaye, P.-M. Hannula, T. Kallio, L. Hupa, M. Lundström, Graphite recovery from waste Li-ion battery black mass for direct re-use, Miner. Eng. 208 (2024) 108587, https://doi.org/10.1016/j.mineng.2024.108587.
[38] S. Hembacher, F.J. Giessibl, J. Mannhart, C.F. Quate, Revealing the hidden atom in graphite by low-temperature atomic force microscopy, Proc. Natl. Acad. Sci. 100 (2003) 12539–12542, https://doi.org/10.1073/pnas.2134173100.
[39] M. Kazemi, K. Liivand, M. Prato, P. Vacek, J. Walmsley, S. Dante, G. Divitini, I. Kruusenberg, Graphite and cobalt recycled from Li-Ion batteries: a valuable raw material for oxygen reduction reaction electrocatalysts, Energy Fuel. 38 (2024) 659–670, https://doi.org/10.1021/acs.energyfuels.3c03495.
[40] M.C. Biesinger, Accessing the robustness of adventitious carbon for charge referencing (correction) purposes in XPS analysis: insights from a multi-user facility data review, Appl. Surf. Sci. 597 (2022) 153681, https://doi.org/10.1016/j.apsusc.2022.153681.
[41] J. Moulder, W. Stickle, P. Sobol, K. Bomben, in: J. Chastain (Ed.), Handbook of X-ray Photoelectron Spectroscopy, Publ Perkin-Elmer Corp, 1992.
[42] F. Rueda, J. Mendialdua, A. Rodriguez, R. Casanova, Y. Barbaux, L. Gengembre, L. Jalowiecki, Characterization of Venezuelan laterites by X-ray photoelectron spectroscopy, J. Electron. Spectrosc. Relat. Phenom. 82 (1996) 135–143, https://doi.org/10.1016/S0368-2048(96)03035-6.
[43] Z.D. Hood, S.P. Adhikari, S.F. Evans, H. Wang, Y. Li, A.K. Naskar, M. Chi, A. Lachgar, M.P. Paranthaman, Tire-derived carbon for catalytic preparation of biofuels from feedstocks containing free fatty acids, Carbon Resour. Convers. 1 (2018) 165–173, https://doi.org/10.1016/j.crcon.2018.07.007.
[44] J.-C. Dupin, D. Gonbeau, P. Vinatier, A. Levasseur, Systematic XPS studies of metal oxides, hydroxides and peroxides, Phys. Chem. Chem. Phys. 2 (2000) 1319–1324, https://doi.org/10.1039/a908800h.
[45] S. Tanaka, M. Taniguchi, H. Tanigawa, XPS and UPS studies on electronic structure of Li2O, J. Nucl. Mater. 283 (2000) 1405–1408, https://doi.org/10.1016/S0022-3115(00)00251-8.
[46] J. Chastain, R.C. King Jr., Handbook of X-ray Photoelectron Spectroscopy, vol. 40, Perkin-Elmer Corp., 1992, p. 25.
[47] N.I. Kovtyukhova, Y. Wang, A. Berkdemir, R. Cruz-Silva, M. Terrones, V.H. Crespi, T.E. Mallouk, Non-oxidative intercalation and exfoliation of graphite by Brønsted acids, Nat. Chem. 6 (2014) 957–963, https://doi.org/10.1038/nchem.2054.
[48] P. Düngen, R. Schlögl, S. Heumann, Non-linear thermogravimetric mass spectrometry of carbon materials providing direct speciation separation of oxygen functional groups, Carbon 130 (2018) 614–622.
[49] A. Ganguly, S. Sharma, P. Papakonstantinou, J. Hamilton, Probing the thermal deoxygenation of graphene oxide using high-resolution in situ X-ray-based spectroscopies, J. Phys. Chem. C 115 (2011) 17009–17019.
[50] J. Collins, G. Gourdin, M. Foster, D. Qu, Carbon surface functionalities and SEI formation during Li intercalation, Carbon 92 (2015) 193–244, https://doi.org/10.1016/j.carbon.2015.04.007.
[51] G. Beamson, D.R. Briggs, High resolution xps of organic polymers, The Scienta esca 300 Database, ICIplc 70 (1993) p. A25.
[52] H. Ramamoorthy, K. Buapan, T. Chiawchan, K. Thamkrongart, R. Somphonsane, Exploration of the temperature-dependent correlations present in the structural, morphological and electrical properties of thermally reduced free-standing graphene oxide papers, J. Mater. Sci. 56 (2021) 15134–15150, https://doi.org/10.1007/s10853-021-06262-w.
[53] K. Li, Y. Zhu, H. Cao, H. Zhang, Y. Wu, X. Li, Z. Xu, Q. Liu, Graphite made from coal by high-temperature treatment: an insight into the nanometric carbon structural evolution, Miner 14 (2024), 2075-163X.
[54] K. Leung, J.L. Budzien, Ab initio molecular dynamics simulations of the initial stages of solid–electrolyte interphase formation on lithium ion battery graphitic anodes, Phys. Chem. Chem. Phys. 12 (2010) 6583–6586, https://doi.org/10.1039/b925853a.
[55] T. Placke, V. Siozios, R. Schmitz, S.F. Lux, P. Bieker, C. Colle, H.-W. Meyer, S. Passerini, M. Winter, Influence of graphite surface modifications on the ratio of basal plane to “non-basal plane” surface area and on the anode performance in lithium ion batteries, J. Power Sources 200 (2012) 83–91, https://doi.org/10.1039/b925853a.
[56] S. Megahed, B. Scrosati, Lithium-ion rechargeable batteries, J. Power Sources 51 (1994) 79–104, https://doi.org/10.1016/0378-7753(94)01956-8.
[57] J.P. Olivier, M. Winter, Determination of the absolute and relative extents of basal plane surface area and “non-basal plane surface” area of graphites and their impact on anode performance in lithium ion batteries, J. Power Sources 97 (2001) 151–155, https://doi.org/10.1016/S0378-7753(01)00527-4.
[58] M. Winter, P. Novák, A. Monnier, Graphites for lithium-ion cells: the correlation of the first-cycle charge loss with the brunauer-emmett-teller surface area, J. Electrochem. Soc. 145 (1998) 428, https://doi.org/10.1149/1.1838281.
[59] J. Seo, J. Im, S. Yoon, K.Y. Cho, Enhancing the performance of Ni-rich lithium metal batteries through the utilization of amine-functionalized 1D/3D nano shields and additives in high-voltage operation, Chem. Eng. J. 470 (2023) 144406, https://doi.org/10.1016/j.cej.2023.144406.
[60] H. Shin, J. Park, A.M. Sastry, W. Lu, Degradation of the solid electrolyte interphase induced by the deposition of manganese ions, J. Power Sources 284 (2015) 416–427, https://doi.org/10.1016/j.jpowsour.2015.03.039.
[61] Z. Guo, Z. Cui, A. Manthiram, Crossover effects of transition-metal ions on lithium-metal anode in localized high concentration electrolytes, Adv. Funct. Mater. (2025) 2501743, https://doi.org/10.1002/adfm.202501743.